npj | quantum materials

Article

Published in partnership with Nanjing University

https://doi.org/10.1038/s41535-026-00889-1

Chiral charge density wave in 1T- and 4Hb-TaS_2: the role of interlayer coupling

Check for updates

Roni Anna Gofman[1,5], Abigail Dishi[1,5], Hyeonhu Bae[2], Yuval Nitzav[1], Ilay Mangel[1], Nitzan Ragoler[1], Sajilesh K P[1], Alex Louat[3], Matthew D. Watson[3], Cephise Cacho[3], Dmitry Marchenko[4], Andrei Varykhalov[4], Irena Feldman[1], Binghai Yan[2] & Amit Kanigel[1] ✉

We use micro-angle-resolved photoemission spectroscopy (micro-ARPES) to investigate chiral charge density waves (CDWs) in 4Hb-TaS_2 with micron-scale spatial resolution. In the 1T layers of 4Hb-TaS_2, we uncover coexisting left- and right-handed CDW domains and resolve four distinct spectral patterns arising from the interplay of chirality and rotational stacking. In contrast, bulk 1T-TaS_2 exhibits uniform chirality. In addition, 4Hb-TaS_2 shows negligible out-of-plane dispersion of the 1T-derived bands, in contrast to the large interlayer coupling observed in bulk 1T-TaS_2. Density Functional Theory (DFT) calculations corroborate this picture, revealing that the interlayer interaction of the chiral order in 4Hb-TaS_2 is nearly two orders of magnitude weaker than in the 1T polytype. Our findings establish 4Hb-TaS_2 as a quasi-two-dimensional platform for exploring tunable chiral CDW phenomena.

Chirality, the property of an object being distinguishable from its mirror image, has profound implications in both fundamental physics and materials science. In crystalline solids, chirality arises when the structure breaks all mirror and inversion symmetries. This results in left and right-handed structural variants, which are related to each other by spatial inversion or reflection.

This structural chirality can lead to a variety of exotic responses, including the anomalous Hall effect[1], natural optical activity[2], and nontrivial topological phenomena[3].

However, chiral behavior can also emerge in systems that preserve inversion symmetry, provided all mirror symmetries are broken. A more accurate description of these systems is that they are pseudo-chiral[4,5] or exhibit an emergent ferro-rotational order[6,7]. In this case, two distinct states can be transformed into one another by a mirror operation.

This scenario is realized, for example, in certain charge-ordered states, where the spontaneous formation of a charge density wave breaks all mirror symmetries of the lattice, resulting in left- and right-handed domains[5,8]. Pseudo-chirality may result in domain-sensitive transport or strain-coupled effects[9]. Understanding such symmetry-breaking patterns is crucial for identifying new correlated phases and unraveling the full richness of emergent phenomena in quantum materials.

In the 1T polytype of tantalum disulfide (TaS_2), a commensurate charge density wave forms at low temperatures, characterized by a $\sqrt{13}\times\sqrt{13}$ superlattice reconstruction relative to the atomic lattice. This reconstruction involves a periodic lattice distortion in which 13 Ta atoms cluster into a “Star of David" (SoD) configuration, with one central Ta atom surrounded by two concentric rings of six atoms each. The formation of these clusters lowers the system’s symmetry by breaking the in-plane mirror operations of the underlying trigonal lattice. Notably, the CDW can adopt one of two degenerate orientations, rotated by either $+13.9^{\circ}$ or -13.9° relative to the atomic lattice vectors. These two configurations are energetically equivalent and related by mirror symmetry.

Among transition-metal dichalcogenides (TMDs), TaS_2 stands out for its rich polymorphism. In addition to the 1T structure discussed above, other polytypes such as 2H, 3R, 4Hb, and 6R have been extensively studied, each exhibiting a distinct set of tunable physical properties.

The 4Hb polytype of TaS_2 crystallizes in a centrosymmetric structure composed of alternating 1H and 1T-TaS_2 layers stacked along the crystallographic *c*-axis (See Fig. 1a). The 1H layers adopt a trigonal prismatic coordination, and appear in two rotational variants, denoted 1H and 1H’, related by a 180° rotation about the *c*-axis. This rotation inverts the in-plane orientation of the trigonal prisms and restores inversion symmetry when considering the full stacking sequence. The 1T layers, which possess intrinsic inversion symmetry, are also present in two rotated forms, 1T and 1T’, related by a 60° in-plane rotation combined with a fractional translation along the *c*-axis. This operation corresponds to a threefold screw axis, that links adjacent 1T layers. The overall 4Hb structure thus preserves global

[1]Department of Physics, Technion, Haifa, Israel. [2]Department of Condensed Matter Physics, Weizmann Institute of Science, Rehovot, Israel. [3]Diamond Light Source, Harwell Science and Innovation Campus, Didcot, UK. [4]Helmholtz-Zentrum Berlin für Materialien und Energie, Berlin, Germany. [5]These authors contributed equally: Roni Anna Gofman, Abigail Dishi. ✉e-mail: amitk@physics.technion.ac.il

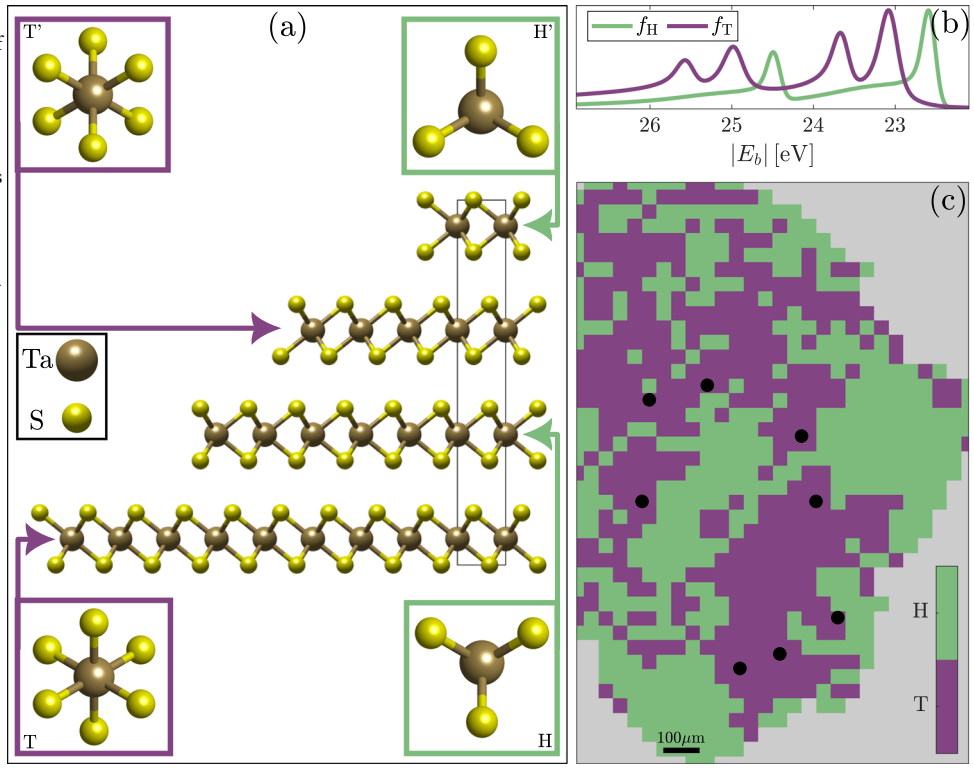

Fig. 1 | Crystal structure and spatial distribution of terminations in 4Hb-TaS_2. a Crystal structure of 4Hb-TaS_2, showing a side view of all layers and separate top views of each individual layer. **b** Calculated Ta 4*f* core-level spectra for the 2H (green) and 1T (purple) polytypes. **c** Spatial distribution map of H (green) and T (purple) domains across a 920 × 1100 μm^2 sample area. Black circles indicate positions in 1T-terminated regions where full $E(k_x, k_y)$ measurements were performed. Representative experimental Ta 4*f* spectra from 1T- and 1H-terminated domains are shown in Supplementary Fig. 1 for comparison with the calculated profiles.

inversion symmetry despite the local asymmetry of the 1H layers, and exhibits both translational and screw symmetries.

As monolayers or even when stacked into separate bulk crystals, the 1H and 1T phases of TaS_2 exhibit fundamentally different properties: the 1H layers are metallic and can host superconductivity, while the 1T layers are correlated insulators. The close proximity of these contrasting layers gives rise to a new emergent quantum state not found in either constituent alone[10,11]. Recent studies have shown that a significant charge transfer occurs from the 1T layers to the 1H layers, effectively doping the latter and modifying their electronic behavior[12]. This proximity, where the correlated electronic state of the 1T layers influences the superconducting behavior of the adjacent 1H layers, is believed to play a key role in stabilizing exotic superconducting phases in 4Hb-TaS_2, including unconventional pairing mechanisms and potentially topological order[13–15].

In this work, we employ micro-angle-resolved photoemission spectroscopy (micro-ARPES) with sub-micron spatial resolution to investigate the electronic structure of 4Hb-TaS_2. This approach enables us to distinguish between the coexisting 1H and 1T surface terminations and to directly probe the layer-specific electronic properties. By focusing on the 1T layers, we reveal the nature of the charge density wave in the 4Hb polytype and uncover key differences from the well-studied bulk 1T-TaS_2.

Results

Termination map based on core-level spectroscopy

Upon cleaving a 4Hb-TaS_2 crystal, terraces of different layers form, leading to heterogeneously terminated domains on the cleaved surface. In conventional ARPES measurements, which typically have spot sizes on the order of 100 μm, data are collected from multiple domains simultaneously. Consequently, the measured band structure represents an average over different domains and incorporates contributions from both the 1T and 1H polytypes.

To distinguish the contributions of different terminations, we employed micro-ARPES, which reduces the averaging over multiple domains inherent to conventional ARPES. With its smaller spot size, approximately 5 μm, this technique allowed us to scan the sample and map the electronic structure on the micrometer scale.

To establish a detailed spatial termination map of the cleaved area, we first analyzed the Ta-4*f* core levels using 80 eV photons. At each point on the sample, we measured within a binding energy range of 22 − 27 eV, which contains the Ta−4*f* core levels. The Ta−4*f* core levels spectra, which is shown in Fig. 1b, can be used to identify the TaS_2 polytype. In the 2H polytype, which features a single Ta site, the Ta−4*f* spectrum displays only a spin-orbit splitting of 1.9 eV. In contrast, in the 1T phase, specifically within the commensurate CDW state, the Ta-4*f* core levels acquire an additional splitting beyond the intrinsic spin-orbit separation. Each spin-orbit component of the Ta- 4*f* line is further split into three sub-components with approximate intensity ratios of 6:6:1, reflecting the three inequivalent Ta sites within the Sod cluster[16–18]. Because the contribution from the central Ta site (1 part) is weak and broadened relative to the outer sites (6 + 6 parts), the line shape appears as a doublet rather than a resolved triplet.

The spectrum of the Ta−4*f* core level at each point on our sample was fitted to a model line shape to determine the polytype at this location on the sample (For more details, see Supplementary Note 1). In Fig. 1c we present a spatial map showing the distribution of different terminations where the H-terminated regions are shown in green and the T-terminated regions in purple.

Spectra from the T-termination

Within the T-terminated domains, we selected specific points (marked as black squares in Fig. 1c) to perform full $E(k_x, k_y)$ measurements, obtaining detailed band structures unique to the individual domain. This approach allowed us to analyze the properties of the 1T layers separately, minimizing cross-domain averaging.

Surprisingly, in T-terminated domains, we observe four distinct spectral patterns. Representative data for these patterns are presented in panels (a–d) of Fig. 2, which shows ARPES intensity maps at the Fermi level and a binding energy ($|E_b| = |E_{kin} - E_f|$) of 500 meV.

At the Fermi level, all four patterns display a weak but clearly visible Fermi surface, reminiscent of the characteristic features of the 2H polytype. A hole pocket appears around the Γ point, accompanied by additional hole-like features near the K and K' points. Within the Γ pocket, we detect spectral

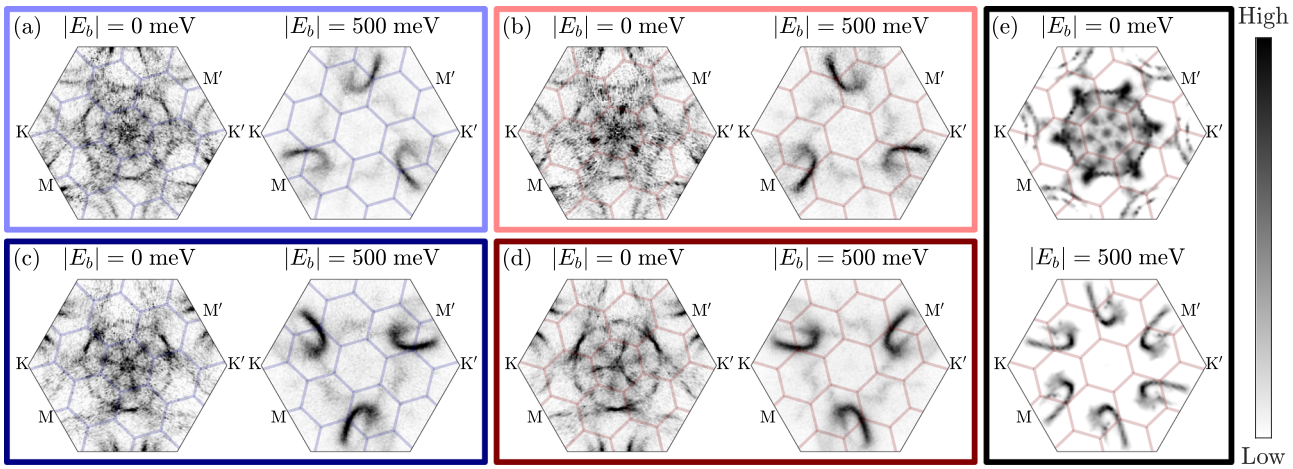

Fig. 2 | 1T-terminated configurations in 4Hb–TaS_2 and corresponding DFT calculations. a–d Energy cuts at the Fermi level and 500 meV below the Fermi energy within the BZ are shown for the four 1T-terminated configurations in 4Hb–TaS_2. Panels within blue rectangles (**a**, **c**) represent left-handed chirality, while those within red rectangles (**b, d**) display right-handed chirality. The red and blue lines outline the mini-BZs associated with the CDW, rotated by − 13° (blue) and + 13° (red) relative to the main BZ. Panels (**a**, **b**) (lighter shades) exhibit threefold symmetry, with the highest intensity centered around the M point. In contrast, Panels (**c**, **d**) (darker shades) are rotated by 60°, with the highest intensity centered around the M' point. **e** DFT calculated constant energy surfaces for a 1T termination in a 4Hb polytype at the same binding energies as in (**a**–**d**).

weight consistent with a Fermi surface derived from the 1T layer, suggesting partial metallization of the otherwise insulating 1T phase. This observation is consistent with previous studies reporting significant charge transfer from the 1T to the 1H layers in 4Hb-TaS_2[12,13].

The 1T-derived Fermi surface includes a small pocket centered at Γ, along with six additional elongated features aligned along directions connecting the Γ-point to the surrounding Γ'-points of the CDW-induced mini Brillouin zones (BZs). The resulting Fermi surface lacks mirror symmetry and thus exhibits chirality. We classify each domain as left- or right-handed based on the handedness of the Fermi surface, which is determined by the orientation of the CDW modulation.

The chirality is set during the formation of the SoD clusters, which define a new lattice rotated by either + 13.9° or − 13.9° relative to the atomic lattice vectors. To illustrate this, we overlay the corresponding CDW-induced mini BZs on the intensity maps in Fig. 2, using red lines for the + 13.9° configuration and blue lines for the − 13.9° case. As indicated by the direction in which the Fermi pockets point, the two panels on the right (enclosed by light and dark red frames) exhibit right-handed chirality, while the two on the left (enclosed by light and dark blue frames) exhibit left-handed chirality.

As the binding energy increases, the spectral features associated with the 2H polytype gradually diminish, and the constant-energy maps begin to resemble those of the 1T insulating phase. Notably, the lower-energy features retain the same chirality as observed at the Fermi surface.

The differences between the four patterns are particularly evident in the intensity maps at 500 meV binding energy. These constant-energy ARPES maps reveal an asymmetric, boomerang-like feature in momentum space, characterized by a skewed bifurcation with unequal arm lengths and intensities, further indicating broken mirror symmetry. In Fig. 2a, c (enclosed by light and dark blue frames), the left arm is more intense, while in b and d (enclosed by light and dark red frames), the right arm dominates. This asymmetry is consistent with the handedness inferred from the orientation of the Fermi pockets.

Although only two chiralities, left- and right-handed, are possible, we observe four distinct spectral patterns in the 1T-terminated domains. This apparent doubling arises from the combination of chirality with a 60° rotation of the spectral intensity pattern. In the constant-energy maps at high binding energy, this manifests as asymmetric features centered either around the M point (Fig. 2a, b, enclosed by light blue and red) or, rotated by 60°, around the M' point (Fig. 2c, d, enclosed by dark blue and red).

We compare the experimental constant-energy maps with those calculated using Density Functional Theory (DFT) for the left-handed CDW configuration. Because DFT does not reproduce absolute quasiparticle binding energies, we apply a small rigid energy alignment of 90 meV. We justify this shift in Supplementary Note 3 through a direct comparison of ARPES and DFT dispersions. The DFT results (shown in Fig. 2e) reproduce key features of the experimental data, including the chiral structure of the 1T-derived Fermi surface within the H-associated Γ pocket and the persistence of this chirality at lower binding energies. However, a notable discrepancy arises: while the experimental maps exhibit a threefold rotational symmetry, the DFT-calculated maps retain the full sixfold symmetry of the underlying lattice. This difference likely originates from matrix-element effects in the ARPES measurements.

ARPES formally measured the single-particle spectral function times the transition dipole matrix element connecting the initial and final states of the emitted electron[19]. The matrix element-induced modulation in the AREPS intensity contains important information about the symmetry and orbital content of the initial state.

Matrix-element-driven intensity asymmetries have been systematically analyzed for trigonal 1T lattices. A recent paper[20] showed that under linearly polarized light, photoemission from 1T-$TiTe_2$ exhibits an apparent reduction of the nominal sixfold symmetry to a threefold pattern, caused by anisotropic dipole coupling to the transition-metal d orbitals. Since the conduction bands in both 1T-$TiTe_2$ and 1T-TaS_2 derive from similarly oriented t_{2g}-like d states, the same photoemission selection rules are expected to apply in TaS_2. Indeed, a comparable threefold modulation has been observed in conventional ARPES measurements of 1T-TaS_2 both above and below the CDW transition temperature[4], confirming that this effect arises purely from lattice and orbital geometry, independent of CDW formation. The photon-energy dependence of the M/M' contrast, strong at 80 eV and weaker at 100 eV (Supplementary Fig. 4), further supports a matrix-element origin for the apparent threefold intensity modulation, while the CDW rotation determines the overall handedness of each domain.

The 4Hb polytype of TaS_2 crystallizes in the $P6_3/mmc$ space group, characterized by a 6_3 screw symmetry that combines a 60° rotation about the c-axis with a half-cell translation ($c/2$) along the stacking direction. This operation enforces the simultaneous presence of 1T and 1T' layers in a fixed alternating geometry, each rotated by 60° relative to the one below, as illustrated in Fig. 1a. Under a fixed linear-polarization geometry, this rotation interchanges the bright and dim M-pocket sets through matrix-element

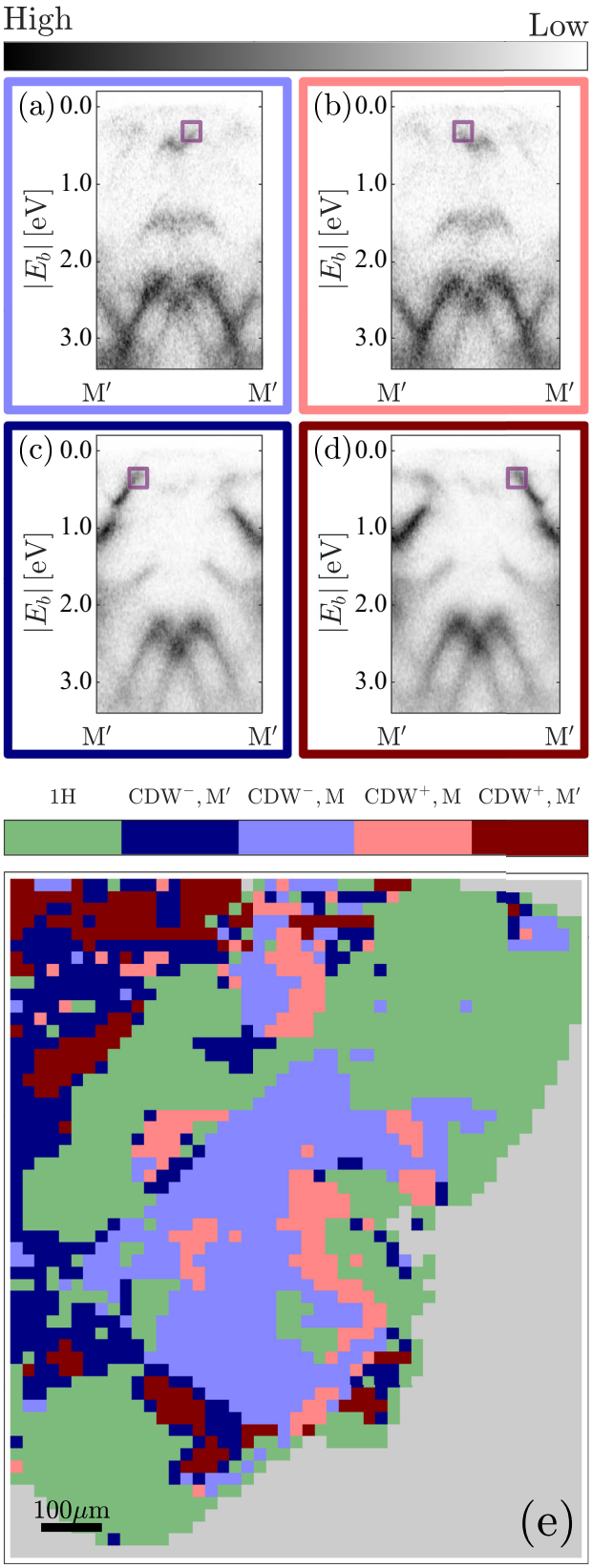

Fig. 3 | Spatial distribution of chiral domains in bulk 4Hb–TaS_2. a–d ARPES spectra acquired along the low-symmetry k-space direction M'-M' (clockwise), for the four distinct 1T-terminated surface configurations of 4Hb–TaS_2. The colors of the frames correspond to those used in Fig. 2. **e** Part of the spatial map in Fig. 1c (pixel size $5 \times 5\ \mu m^2$) now showing the distribution of the four configurations, with red and blue shades matching those of the frames in (**a**–**d**) and in Fig. 2. The green regions are H-terminated, while the grey areas are outside the cleaved sample. This spatial map was scanned with the detector aligned along the low symmetry line M'-M', and intensity differences between the purple rectangles identified each 1T-termination form.

selection, giving rise to two intensity patterns related by 60°. Combining these two rotational variants with the two possible CDW chiralities naturally produces the four distinct spectral patterns observed in Fig. 2.

As shown in Fig. 2, we observe both left- and right-chirality spectral patterns in the 1T and 1T' domains, indicating that there is no simple correlation between the layer type (1T or 1T') and the CDW angle.

Chiral domain spatial mapping

To assess the prevalence of each 1T spectral pattern, we use micro-ARPES to map the sample. While it is difficult to identify the handedness from the spectra along a high symmetry line (Supplementary Fig. 5) the low-symmetry cut from M′ to M′ allows a clear determination of the chirality and the relative rotation (T vs. T'). So, at each point, we measured the dispersion in momentum space along this direction. In Fig. 3a–d, we present the corresponding spectra for each of the four 1T spectral patterns, with colors matching those in Fig. 2.

In Fig. 3e, we show a map illustrating the distribution of 1T patterns across the sample. In this region, approximately 71% of the 1T domains exhibit left-handed chirality (dark and light blue), and around 57% display a 3-fold symmetry centered at the M-point (light blue and red). In another sample, these values were 78% and 55%, respectively.

From the same real-space chirality map, we quantitatively extract the domain-size distribution by identifying connected regions of uniform chirality. Defining a characteristic linear domain size as $\ell = \sqrt{A}$, where A is the domain area, we obtain a mean length scale of 88.2 μm with an interquartile range of 53–102 μm (Supplementary Note 6). These values establish the mesoscale character of the chiral CDW domains in 4Hb–TaS_2.

For other samples, we did not perform a full spatial scan at this orientation but instead selected several points within the 1T domains and identified the spectral patterns at each location. Across all our samples, we consistently observed all four spectral forms: left- and right-handed CDW states in both 1T and 1T' domains. Roughly half of the examined samples showed a majority of left-handed domains, while right-handed ones dominated the other half; therefore, neither handedness is energetically favored.

The behavior we found in the 1T layers of 4Hb-TaS_2 should be compared to the case of bulk 1T-TaS_2. In Fig. 4a, we show a total-intensity map measured using micro-ARPES. The white circles represent points at which we performed a full $E(k_x, k_y)$ measurement and determined the corresponding spectral patterns. In Fig. 4b, c, we present representative constant-energy intensity maps at the Fermi level (b) and at a binding energy of 500 meV (c). In this sample, all measurements consistently reveal a mono-domain structure exhibiting left-handed chirality and a three-fold intensity symmetry centered at the M' point. Remarkably, all 1T-TaS_2 samples we examined display uniform chirality across the entire measured area, which can span several mm^2. Previous ARPES studies[4,21] and Raman measurements[4,6] support this, confirming homogeneous chirality over large areas in 1T-TaS_2. This well-established behavior in the 1T polytype stands in sharp contrast to the multi-domain chiral structure revealed in the 1T layer of all our 4Hb-TaS_2 samples.

Out-of-plane dispersion

We continue our comparison of the electronic spectra between the 1T-dominated domains within the 4Hb polytype and the bulk 1T polytype, shifting our attention to the out-of-plane dispersion ($k_\perp$). Micro-ARPES was employed for the measurement in the 1T-dominated domains in 4Hb-TaS2, while large-spot ARPES was used to measure the dispersion in bulk 1T-TaS_2.

In both experiments, the analyzer slit was aligned along the surface projected K'-Γ'-K crystallographic direction. Panels (a, b) of Fig. 5 show the

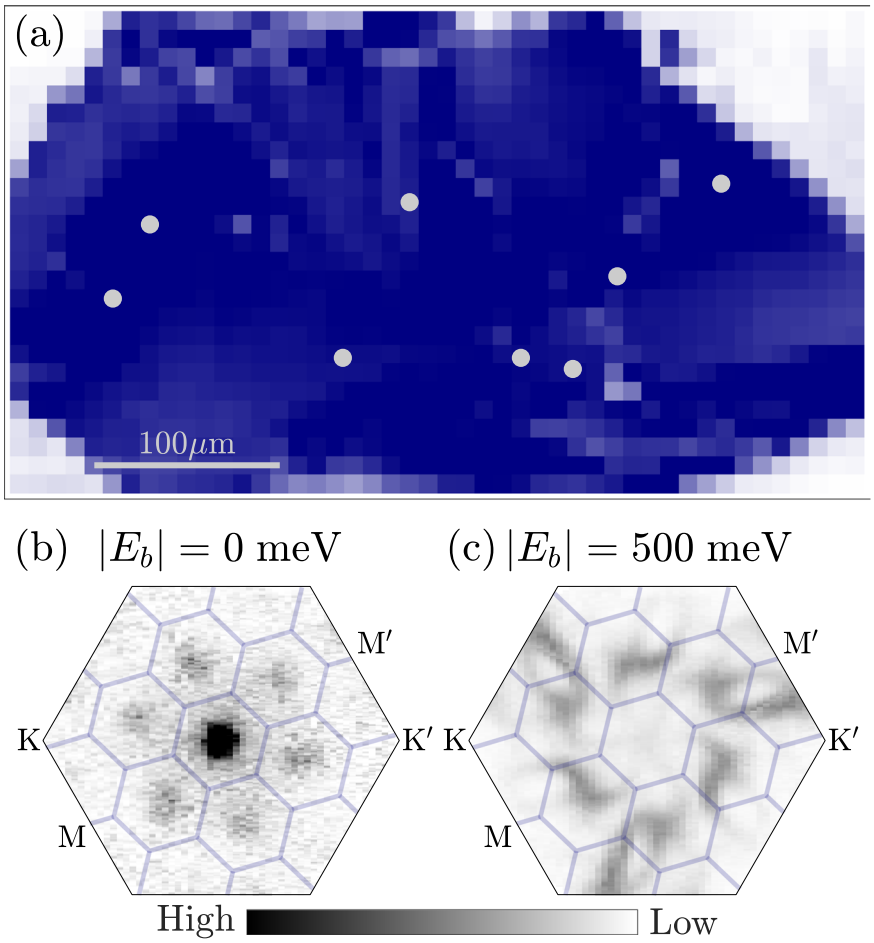

Fig. 4 | Uniform chiral domain in bulk 1T–TaS_2. **a** A spatial map of a bulk 1T–TaS_2 sample. The color represents the total intensity summed over the ARPES detector. The blue region corresponds to a cleaved area of approximately 250 × 450 μm^2 with a pixel size of 10 × 10 μm^2. The white circles indicate points where a full $E(k_x, k_y)$ scan was measured. **b**, **c** ARPES constant energy maps, symmetrized with a 120° rotation at E_b = 0 and 500 meV, respectively. All eight maps measured at different locations on the sample exhibit the same spectral pattern.

corresponding spectra for 4Hb- and 1T-TaS_2, respectively. To probe the $k_\perp$ dispersion, we varied the photon energy: from 40 eV to 100 eV for 4Hb polytype, covering approximately six BZs, and from 42 eV to 144 eV for 1T, covering about 2.5 BZs. Additional details on the determination of $k_\perp$ values are provided in Supplementary Note 7.

We compare the $k_\perp$ dispersion at an in-plane momentum of $k_\parallel = -0.77$ Å^{-1}, moving away from the Γ point toward the K point, as indicated by the vertical lines in panels (a) and (b) of Fig. 5. At this momentum, a 1T-derived band is observed at a binding energy of approximately 1 eV in 1T-TaS_2, and around 800 meV in the 1T domain of 4Hb-TaS_2. In panels Fig. 5c, d, we show the corresponding $k_\perp$ dispersion of this band in the 1T-dominated domain and the bulk 1T phase, respectively. The markers indicate the peak energy of the energy distribution curves (EDCs) at each $k_\perp$. In the bulk 1T-TaS_2 sample, this band exhibits a pronounced out-of-plane dispersion with a bandwidth of approximately 120 meV, consistent with previous reports[22,23] and DFT calculations[24]. In contrast, the same band in the 1T-terminated domain of 4Hb-TaS_2 shows negligible $k_\perp$ dependence, with a bandwidth smaller than 20 meV. We examined additional 1T-derived bands at various in-plane momenta and found that all exhibit similarly flat $k_\perp$ dispersion in 4Hb-TaS_2 (Supplementary Fig. 7).

Discussion

Bulk 1T–TaS_2 provides a well-established example of a three-dimensional CDW system, where the out-of-plane bandwidth is significant, and the CDW stacking sequence strongly influences the electronic and structural ground states[24]. This 3D interlayer coherence rigidly locks the CDW pattern across layers, giving rise to the single, millimeter-scale chiral domain that has been repeatedly observed in bulk 1T–TaS_2[4,25–28]. Our findings are consistent with this picture: bulk 1T-TaS_2 exhibits the expected k_z dispersion characteristic of a three-dimensional CDW system.

In contrast, our μ-micro-ARPES measurements on 4Hb–TaS_2 reveal a very small out-of-plane dispersion in the 1T-derived bands, demonstrating that the 1T layers are electronically quasi-two-dimensional. Previous X-ray diffraction work provided initial evidence for a quasi-2D CDW in the 1T layers[29], and our spectroscopic results are consistent with this picture while offering direct, momentum-resolved insight and revealing both the coexistence of opposite chiralities and their characteristic domain sizes of 10–100 μm.

The two-to-three-order-of-magnitude reduction in chiral domain size observed in 4Hb–TaS_2 compared to bulk 1T–TaS_2 can be understood in terms of the much weaker interlayer coupling in the 4Hb polytype, which effectively confines electrons within individual 1T layers. In this quasi-2D regime, chiral domain walls can form independently in each layer without requiring interlayer alignment, enabling the flexible, layer-resolved textures revealed in our μ-micro-ARPES maps. This interpretation is consistent with previous observations, in disordered 1T samples, showing that the intervening 1H layers decouple adjacent 1T units, allowing them to adopt different chiralities, whereas directly stacked 1T layers tend to exhibit identical chirality[30].

Our DFT calculations further support this picture. The energy difference between homochiral and heterochiral stacking configurations in 4Hb-TaS_2 is only a few meV per SoD, indicating that the interlayer alignment of the chiral order is only weakly constrained (see Supplementary Material 8 for details). This small energy scale is consistent with the possibility of layer-to-layer variations in chirality. By contrast, in bulk 1T-TaS_2 the cost of reversing the chirality of a single layer is on the order of hundreds of meV per SoD[25], enforcing a rigid interlayer alignment and precluding the formation of independent, layer-confined chiral domain walls.

Taken together, these results link the magnitude of interlayer coupling to the observed chiral length scale. While bulk 1T–TaS_2 exhibits strong

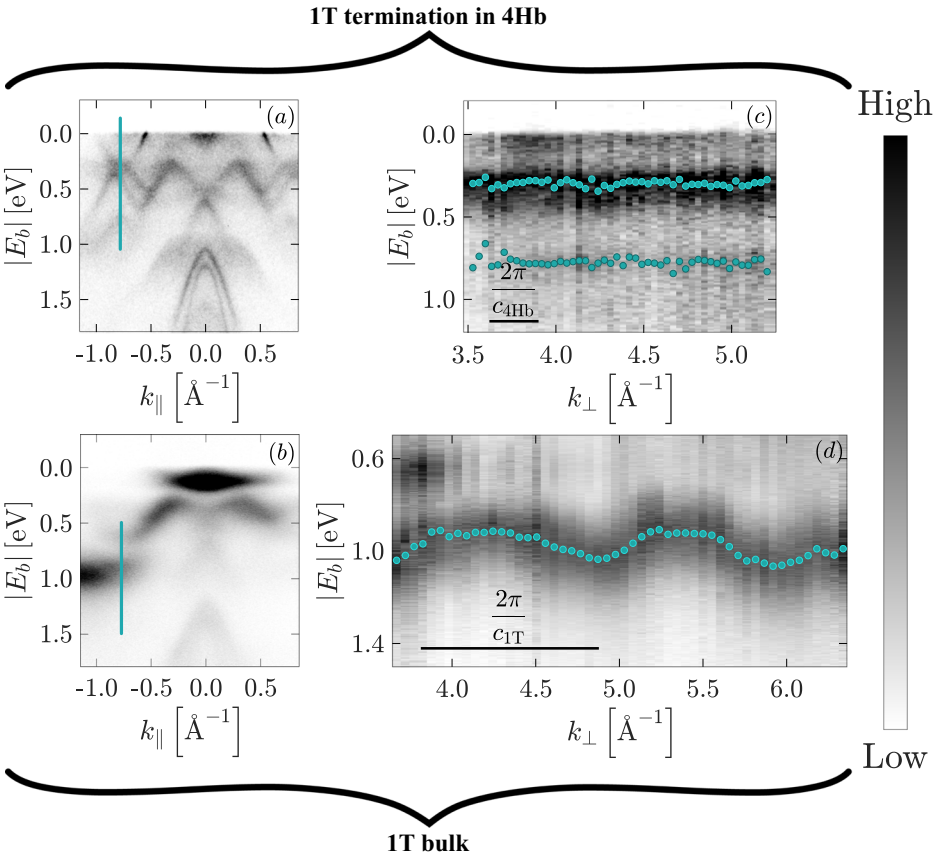

Fig. 5 | Comparison of out-of-plane electronic dispersion between the 1T termination in 4Hb–TaS_2 and bulk 1T. a Dispersion along the surface-projected K'--Γ--K direction for the 1T termination in bulk 4Hb, using 62 eV photon energy. The vertical line marks the $k_\parallel$ value used in (**c**). **b** Same as (**a**), but for bulk 1T. The vertical line marks the $k_\parallel$ value used in (**d**). **c** $k_\perp$ dispersion of the 1T termination in bulk 4Hb at $k_\parallel = -0.77$ Å^{-1}, corresponding to the vertical line in (**a**). Cyan markers denote EDC peak positions as a function of $k_\perp$. **d** Same as (**c**), but for bulk 1T at the $k_\parallel$ value marked in (**b**).

interlayer locking that stabilizes millimeter-scale single-domain chirality[4,25], 4Hb–TaS_2 is characterized by a much smaller interlayer energy scale, permitting layer-confined chirality variations. The substantially reduced domain size observed in our real-space μ-micro-ARPES maps is therefore consistent with this weakened interlayer locking.

An additional consequence of this reduced dimensionality is that long-range chiral order itself becomes unstable. In a quasi-two-dimensional system, the loss of interlayer coherence lowers the energetic cost of creating chiral boundaries, making it possible for domain walls to form not only between layers but also *within* a single 1T layer. Such intra-layer coexistence of opposite chiralities has been directly observed in 4Hb-TaS_2 by STM[15].

These observations identify interlayer coupling as the central parameter controlling the stability and tunability of chiral order in TaS_2 polytypes, with potential implications for functional control. In bulk 1T-TaS_2, chiral domain walls can be induced only when the coupling is locally weakened, for example, through stacking faults created by ultrafast excitation, rapid quenching, or voltage-driven restructuring in thin flakes[26–28,31]. In 4Hb, where the intrinsic interlayer coupling is already much smaller, the same principle naturally gives rise to multiple chiral domains at the mesoscale. This reduced interlayer coupling in 4Hb-TaS_2 lowers the energetic cost of nucleating and moving chiral domain walls, making switching between distinct chiral configurations more local and potentially more accessible than in bulk 1T systems, where switching has been demonstrated but is constrained by strong interlayer locking[6]. From this perspective, interlayer coupling serves as an effective control knob: further reducing it in 1T, for instance, by intercalation[32] or tensile strain, should promote additional chiral boundaries and increase switchability, while enhancing it in 4Hb, such as under applied pressure, is expected to suppress domain walls and stabilize a uniform chiral state. Recognizing interlayer coupling as the microscopic parameter governing domain morphology provides a coherent framework for engineering chiral textures and manipulating their switching behavior in layered CDW materials.

Beyond the present material, the ability to combine real-space selectivity with momentum resolution makes μ-micro-ARPES broadly applicable to complex systems with spatially heterogeneous electronic order. Examples include multi-domain charge- or spin-density-wave materials, as demonstrated here, twisted or moiré van der Waals heterostructures with locally varying stacking configurations, and layered systems in which stacking faults or polytype intergrowths naturally generate electronic domains[23,33,34]. More generally, spatial variations evident in core-level spectroscopy or growth-dependent shifts raise the question of whether similar heterogeneity exists in the valence and conduction bands that govern low-energy electronic behavior[35]. In such cases, conventional ARPES averages over inequivalent regions, whereas μ-micro-ARPES enables direct access to the local electronic structure of individual domains, interfaces, or textures.

Finally, although our focus is the mirror-symmetry-breaking chirality of the normal-state CDW, our results are relevant to ongoing discussions of possible chiral superconductivity in 4Hb-TaS_2. Prior work from our group reported a π-shifted Little-Parks effect[14], and a similar π shift was recently observed in 2H-TaS_2 intercalated with chiral molecules[36]. A theoretical framework has likewise proposed a coupling between chiral molecules, chiral CDW textures, and time-reversal-symmetry breaking in TaS_2-based systems[37]. In this context, our work provides a missing ingredient: a spatially resolved map of chiral CDW domains in the normal state. Because such mesoscale textures shape the local electronic environment in which superconductivity forms, our measurements offer essential input for future models linking CDW chirality to unconventional pairing.

To summarize, our micro-ARPES measurements reveal that the 1T layers in 4Hb-TaS_2 host coexisting left- and right-handed chiral CDW domains with characteristic sizes of tens of microns. By mapping these domains in real space and resolving their momentum-space signatures, we can distinguish the contributions of the 1T and 1T' layers and identify four distinct spectral patterns arising from the combination of chirality and the intrinsic 60° degree rotation between adjacent 1T layers. This contrasts with

bulk 1T-TaS_2, which typically forms a single macroscopic chiral domain. A direct comparison between the two polytypes shows that the 1T-derived bands in 4Hb-TaS_2 exhibit negligible out-of-plane dispersion, indicating a strongly reduced interlayer coupling relative to bulk 1T-TaS_2. This weakened coupling enables independently ordered chiral textures and explains the emergence of multiple chiral domains at the mesoscale. These findings identify dimensionality and interlayer coupling as key parameters governing the stability of long-range chiral CDW order and demonstrate the power of micro-ARPES for resolving chiral textures in layered materials. The domain-resolved chiral landscape reported here provides essential microscopic input for future studies of the interplay between CDW chirality, electronic correlations, and unconventional superconductivity in TaS_2-based systems.

Methods

Crystal growth

4Hb crystals were synthesized using the chemical vapor transport technique. Se was incorporated during growth to stabilize the 4Hb phase and enhance the properties of the superconducting phase. Se concentrations in the analyzed samples ranged from 0% to 5%. The grown crystals were then cut into pieces, typically a few millimeters wide and approximately 0.5 mm thick.

Micro-ARPES measurements

Micro-ARPES measurements were performed at the I05 beamline of the Diamond Light Source. Samples were introduced into an ultra-high vacuum (UHV) chamber and maintained at approximately 40 K. They were cleaved in situ to ensure clean surfaces. The beam, with a spot size of about $5 \times 5\ \mu m^2$ and linear horizontal (LH) polarization, was used with photon energies ranging from 60 to 100 eV.

Out-of-Plane ARPES measurements

Out-of-plane ARPES measurements on bulk 1T samples were conducted at the ARPES One-Square beamline at the BESSY-II synchrotron. These experiments were carried out under UHV conditions, with pressures maintained below 5×10^{-11} torr, and at an approximate temperature of 40 K. Beam spot size was about 100 microns.

DFT calculations

Density functional theory (DFT) calculations were performed with the VASP software using the projector-augmented wave method[38]. We employed the Perdew-Burke-Ernzerhof (PBE) exchange-correlation functional[39], while van der Waals interactions were accounted for via the DFT-D3 scheme with Becke-Johnson damping[40]. To model the 4Hb stacking, we constructed $\sqrt{13} \times \sqrt{13}$ supercells for bulk 4Hb-TaS_2 and for 1T/1H bilayer structures, choosing either left- or right-handed chirality. For the heterochiral 4Hb-TaS_2 calculation, see Supplemental Note 8. The bilayer model was used to compute the Fermi surface of the exposed 1T layer. Spin-orbit coupling was included in these Fermi surface calculations. A plane wave energy cutoff of 400 eV was adopted. The electronic energy convergence criterion was set to 10^{-7} eV. Ionic positions were relaxed until all residual Hellmann-Feynman forces were smaller than 1 meV/Å. Band structure unfolding was carried out using the VASPKIT code[41].

Data Availability

The data that support the findings of this study are provided in the main text and the Supplementary Information. The original data is available from the corresponding author upon request.

Received: 24 August 2025; Accepted: 21 April 2026;
Published online: 05 May 2026

References

1. Nagaosa, N., Sinova, J., Onoda, S., MacDonald, A. H. & Ong, N. P. Anomalous Hall effect. *Rev. Mod. Phys.* **82**, 1539–1592 (2010).
2. Barron, L. D.*Molecular light scattering and optical activity* (Cambridge University Press, 2009).
3. Kharzeev, D. E. The chiral magnetic effect and anomaly-induced transport. *Prog. Part. Nucl. Phys.* **75**, 133–151 (2014).
4. Yang, H. F. et al. Visualization of chiral electronic structure and anomalous optical response in a material with chiral charge density waves. *Phys. Rev. Lett.* **129**, 156401 (2022).
5. Louat, A. et al. The pseudochiral Fermi surface of α-rui3. *Commun. Phys.* **7**, 43 (2024).
6. Liu, G. et al. Electrical switching of ferro-rotational order in nanometre-thick 1T-TaS_2 crystals. *Nat. Nanotechnol.* **18**, 854–860 (2023).
7. Jin, W. et al. Observation of a ferro-rotational order coupled with second-order nonlinear optical fields. *Nat. Phys.* **16**, 42–46 (2020).
8. Guo, X. et al. Ferrorotational domain walls revealed by electric quadrupole second harmonic generation microscopy. *Phys. Rev. B* **107**, L180102 (2023).
9. Yan, B. Structural chirality and electronic chirality in quantum materials. *Ann. Rev. Mater. Res.* **54**, 97–115 (2024).
10. Ribak, A. et al. Chiral superconductivity in the alternate stacking compound 4Hb-TaS_2. *Sci. Adv.* **6**, eaax9480 (2020).
11. Manzeli, S., Ovchinnikov, D., Pasquier, D., Yazyev, O. V. & Kis, A. 2D transition metal dichalcogenides. *Nat. Rev. Mater.* **2**, 1–15 (2017).
12. Almoalem, A. et al. Charge transfer and spin-valley locking in 4Hb-TaS_2. *npj Quantum Mater.* **9**, 36 (2024).
13. Nayak, A. K. et al. Evidence of topological boundary modes with topological nodal-point superconductivity. *Nat. Phys.* **17**, 1413–1419 (2021).
14. Almoalem, A. et al. The observation of Π-shifts in the little-parks effect in 4Hb-TaS_2. *Nat. Commun.* **15**, 4623 (2022).
15. Silber, I. et al. Two-component nematic superconductivity in 4Hb-TaS_2. *Nat. Commun.* **15**, 824 (2024).
16. Hughes, H. & Scarfe, J. Lineshapes in core-level photoemission from metals: I. theory and computational analysis. *J. Phys.: Condens. Matter* **8**, 1421 (1996).
17. Hughes, H. & Scarfe, J. Lineshapes in core-level photoemission from metals: II. and its transition metal intercalates. *J. Phys.: Condens. Matter* **8**, 1439 (1996).
18. Hughes, H. & Scarfe, J. Lineshapes in core-level photoemission from metals: III. site-dependent screening in the charge density wave materials 1t-and. *J. Phys.: Condens. Matter* **8**, 1457 (1996).
19. Damascelli, A. Probing the electronic structure of complex systems by ARPES. *Phys. Scr.* **2004**, 61 (2004).
20. Beaulieu, S. et al. Unveiling the orbital texture of 1T-$TiTe_2$ using intrinsic linear dichroism in multidimensional photoemission spectroscopy. *npj Quantum Mater* **6**, 93 (2021).
21. Wang, Y. et al. Band insulator to mott insulator transition in 1T-TaS_2. *Nat. Commun.* **11**, 4215 (2020).
22. Ngankeu, A. S. et al. Quasi-one-dimensional metallic band dispersion in the commensurate charge density wave of 1 T-TaS_2. *Phys. Rev. B* **96**, 195147 (2017).
23. Nitzav, Y. et al. Emergence of a Fermi surface in the current-driven hidden state of 1T-TaS_2. *Phys. Rev. B* **113**, 085104 (2026).
24. Ritschel, T., Berger, H. & Geck, J. Stacking-driven gap formation in layered 1T-TaS_2. *Phys. Rev. B* **98**, 195134 (2018).
25. Zhao, Y. et al. Spectroscopic visualization and phase manipulation of chiral charge density waves in 1T-TaS_2. *Nat. Commun.* **14**, 2223 (2023).
26. Zong, A. et al. Ultrafast manipulation of mirror domain walls in a charge density wave. *Sci. Adv.* **4**, eaau5501 (2018).
27. de la Torre, A. et al. Dynamic phase transition in 1T-TaS_2 via a thermal quench. *Nat. Phys.* **21**, 1267–1274 (2025).
28. Riffle, J. V., de la Torre, A., Plumb, K. W. & Hollen, S. M. Cooling rate dependence of charge density wave phases in 1T-TaS_2 studied by scanning tunneling microscopy and x-ray diffraction. *AIP Adv.* **14**, 105303 (2024).

29. Yang, F. Z. et al. Charge density waves in the 2.5-dimensional quantum heterostructure. *Phys. Rev. B* **111**, L041101 (2025).
30. Husremović, S. et al. Encoding multistate charge order and chirality in endotaxial heterostructures. *Nat. Commun.* **14**, 6031 (2023).
31. Qi, W. et al. Temperature induced, reversible switching of ferro-rotational order coupled to superlattice commensuralibity. *Nano Lett.* **24**, 13134–13139 (2024).
32. Meyer, S. F., Howard, R. E., Stewart, G. R., Acrivos, J. V. & Geballe, T. H. Properties of intercalated 2H-$NbSe_2$, 4Hb-TaS_2, and 1T-TaS_2. *J. Chem. Phys.* **62**, 4411–4419 (1975).
33. Mo, S. et al. Resonant interlayer coupling in $NbSe_2$-graphite epitaxial moiré superlattices. *Adv. Mater.* **38**, e11262 (2025).
34. Wang, Q. et al. Metal–insulator transition driven by the interplay of vacancies and charge orders in square-net materials $GdSb_xTe_{2-x-\delta}$. *Adv. Mater.* **38**, e10303 (2025).
35. Kalläne, M. et al. Stabilization of the misfit layer compound $(PbS)_{1.13}TaS_2$ by metal cross substitution. *Phys. Rev. Lett.* **100**, 065502 (2008).
36. Wan, Z. et al. Unconventional superconductivity in chiral molecule-TaS_2 hybrid superlattices. *Nature* **632**, 69 (2024).
37. Mandal, S. & Liu, C.-X. Pair-mixing induced time-reversal-breaking superconductivity. arXiv preprint arXiv:2511.04629. https://arxiv.org/abs/2511.04629. (2025).
38. Kresse, G. & Joubert, D. From ultrasoft pseudopotentials to the projector augmented-wave method. *Phys. Rev. B* **59**, 1758 (1999).
39. Perdew, J. P., Burke, K. & Ernzerhof, M. Generalized gradient approximation made simple. *Phys. Rev. Lett.* **77**, 3865 (1996).
40. Grimme, S., Ehrlich, S. & Goerigk, L. Effect of the damping function in dispersion corrected density functional theory. *J. Computational Chem.* **32**, 1456–1465 (2011).
41. Wang, V., Xu, N., Liu, J.-C., Tang, G. & Geng, W.-T. Vaspkit: A user-friendly interface facilitating high-throughput computing and analysis using VASP code. *Computer Phys. Commun.* **267**, 108033 (2021).

Acknowledgements

We acknowledge Diamond Light Source, located on the Harwell Science and Innovation Campus near Didcot, Oxfordshire, UK, for providing synchrotron radiation beamtime at the I05 beamline. We thank Helmholtz-Zentrum Berlin's ARPES One-Square beamline for allocating synchrotron radiation beamtime. The work at the Technion was supported by the Israeli Science Foundation under grant number ISF-568/25.

Author contributions

R.A.G. and A.D. performed the ARPES measurements and analyzed the data. Y.N., I.M. and N.R. helped with ARPES measurements. I.F. and S.K.P. synthesized the single crystals. H.B. and B.Y. carries out the DFT calculations. A.L., M.D.W., C.C., D.M., A.V. provided support at the synchrotron beam-lines. A.K. conceived the project. R.A.G., A.D. and A.K. wrote the manuscript with contributions from all authors.

Competing interests

The authors declare no competing interests.

Additional information

Supplementary information The online version contains supplementary material available at https://doi.org/10.1038/s41535-026-00889-1.

Correspondence and requests for materials should be addressed to Amit Kanigel.

Reprints and permissions information is available at http://www.nature.com/reprints

Publisher's note Springer Nature remains neutral with regard to jurisdictional claims in published maps and institutional affiliations.

Open Access This article is licensed under a Creative Commons Attribution-NonCommercial-NoDerivatives 4.0 International License, which permits any non-commercial use, sharing, distribution and reproduction in any medium or format, as long as you give appropriate credit to the original author(s) and the source, provide a link to the Creative Commons licence, and indicate if you modified the licensed material. You do not have permission under this licence to share adapted material derived from this article or parts of it. The images or other third party material in this article are included in the article's Creative Commons licence, unless indicated otherwise in a credit line to the material. If material is not included in the article's Creative Commons licence and your intended use is not permitted by statutory regulation or exceeds the permitted use, you will need to obtain permission directly from the copyright holder. To view a copy of this licence, visit http://creativecommons.org/licenses/by-nc-nd/4.0/.

© The Author(s) 2026